A real-time approach to frequency-mixing spectroscopies: application to sum and difference frequency generation in two-dimensional crystals

Mike N. Pionteck[1*], Myrta Grüning[2,3], Simone Sanna[1], Claudio Attaccalite[3,4]

1 Institut für Theoretische Physik and Center for Materials Research (LaMa), Justus-Liebig-Universität Gießen, 35392 Gießen, Germany
2 School of Mathematics and Physics, Queen's University Belfast, Belfast BT7 1NN, United Kingdom
3 European Theoretical Spectroscopy Facilities (ETSF)
4 CNRS/Aix-Marseille Université, Centre Interdisciplinaire de Nanoscience de Marseille UMR 7325 Campus de Luminy, 13288 Marseille cedex 9, France
* Mike.Pionteck@theo.physik.uni-giessen.de

Abstract

We propose a computational framework to extract non-linear response functions from real-time simulations in presence of more than one external field. We apply this approach to the calculation of sum frequency generation (SFG) and difference frequency generation (DFG). SFG and DFG are second-order nonlinear processes where two lasers with frequencies ω_1 and ω_2 combine to produce a response at frequency $\omega = \omega_1 \pm \omega_2$. Compared with other nonlinear responses such as second-harmonic generation, SFG and DFG allow for tunability over a larger range. Moreover, the optical response can be enhanced by selecting the two laser frequencies in order to match specific electron-hole transitions.
To assess the approach, we calculate the SFG and DFG of two-dimensional crystals, *h*-BN and MoS_2 monolayers, from real-time solution of an effective Schrödinger equation. Within the effective Schrödinger equation, one can select from various levels of theory for the effective one-particle Hamiltonian to account for local-field effects and electron-hole interactions. We compare results obtained within the independent-particle picture and including many-body effects. Such comparison allows us to identify and characterize excitonic features in the obtained spectra. Additionally, we demonstrate that our approach can also extract higher-order response functions, such as field-induced second-harmonic generation. We provide an example using *h*-BN bilayer.

Contents

effective many-body Hamiltonian. Different correlation effects can be accounted for by constructing the corresponding effective Hamiltonian. The simplest approximation for the effective Hamiltonian we consider in this work is the independent particle approximation (IPA) describing the unperturbed (zero-field) Kohn-Sham system [18]

$$H^{\rm MB} \equiv H^{\rm KS} = -\frac{\hbar^2}{2m}\sum_i \nabla_i^2 + V_{\rm eI} + V_{\rm h}[\rho^0] + V_{\rm xc}[\rho^0] = \sum_i \varepsilon_{n,\mathbf{k}} \left|u_{n,\mathbf{k}}\right\rangle \left\langle u_{n,\mathbf{k}}\right| , \qquad (2)$$

no indentation

where $\hat{V}_{\rm eI}$ is the electron-ion interaction, $\hat{V}_{\rm H}[\rho^0]$ and $\hat{V}_{\rm xc}[\rho^0]$ are respectively the Hartree and exchange-correlation potentials evaluated at the unperturbed ground-state electron density ρ^0, $\varepsilon_{n,\mathbf{k}}$ the Kohn-Sham energies (eigenvalues) and $|u_{n,\mathbf{k}}\rangle$ the periodic part of the Kohn-Sham wavefunctions. The Hamiltonian in Eq. (2) has two main shortcomings. First, the band gaps obtained from the Kohn-Sham energies are systematically underestimated—yielding to an overall underestimation of the optical gap. Second, the response of the density-functional potentials to the change in the density is missing and so are local-field effects and quasi-particle excitations. The former shortcoming is corrected by introducing a state-dependent scissor operator term,

space

$$\Delta\hat{H}_{\mathbf{k}} = \sum_n \Delta_{n\mathbf{k}} \left|u_{n,\mathbf{k}}\right\rangle \left\langle u_{n,\mathbf{k}}\right| , \qquad (3)$$

no indentation

where state-dependent $\Delta_{n\mathbf{k}}$ is the scissor operator. That is, considering the Kohn-Sham energies as the zero-order approximation to quasiparticle energies, the scissor operator introduces a first order correction. Such correction can be obtained from first-principles within the so-called *GW* approximation derived from many-body perturbation theory [19] (a simpler approach is to have a single scissor operator chosen to reproduce e.g. the experimental fundamental band gap). To address the second shortcoming, we include the fluctuation of the Hartree potential (Eq. (2)) generated by the variation of the electron density $\Delta\rho = \rho - \rho^0$ induced by the external fields [12], and the screened-exchange self-energy term $\Sigma_{\rm SEX}[\Delta\gamma]$ where $\Delta\gamma$ is the fluctuation of the density matrix [20]. This latter term is a nonlocal operator which accounts for the screened electron-hole attraction and introduces excitonic effects. We so obtain the following effective Hamiltonian,

$$H^{\rm MB}_{\mathbf{k}} \equiv H^{\rm KS}_{\mathbf{k}} + \Delta H_{\mathbf{k}} + V_{\rm h}(\mathbf{r})[\Delta\rho] + \Sigma_{\rm SEX}[\Delta\gamma] , \qquad (4)$$

which is the most accurate Hamiltonian considered in this work and is known as time-dependent adiabatic GW (TD-aGW)[1] approximation [20]. This Hamiltonian (Eq. (4)) is built in such a way to reproduce the band structure and the response functions of the the standard *GW* + BSE approach [19, 22]. This has been shown in the limit of small perturbation both analytically and numerically in Ref. [20].

From the solutions $|v_{m\mathbf{k}}\rangle$ in Eq. (1), we calculate the real-time polarization along the lattice vector $\mathbf{a}$ as [13]:

$$\mathcal{P}_{\parallel}(t) = -\frac{ef|\mathbf{a}|}{2\pi V}{\rm Im}\,\log\prod_{\mathbf{k}}^{N_{\mathbf{k}}-1} {\rm det}S\left(\mathbf{k},\mathbf{k}+\mathbf{q};t\right) , \qquad (5)$$

where $S(\mathbf{k},\mathbf{k}+\mathbf{q};t)$ is the overlap matrix between the time-dependent valence states $|v_{n\mathbf{k}}\rangle$ and $|v_{m\mathbf{k}+\mathbf{q}}\rangle$, V is the unit cell volume, f is the spin degeneracy, $N_{\mathbf{k}}$ is the number of

[1] Notice that the TD-aGW approximation was called TD-BSE, TD-SEX or TD-HSEX in previous publications [10, 20, 21].

where $\mathcal{F}_i^{(n)} \equiv \exp\left[-i\omega^{(n)}t_i\right]$. The solution of the $(2S+1)$ system of linear equations [Eq.(12)] outputs the $C_\alpha^{(n)}$, from which in turn one gets the n^{th}-order susceptibility by dividing by the n^{th} power of the α component of $\boldsymbol{\mathcal{E}}_0$. The nonlinear susceptibilities converge rapidly with S: in Ref. [12] it was found that second-order susceptibilities converge already with $S = 4$ and third-order susceptibilities with $S = 6$.

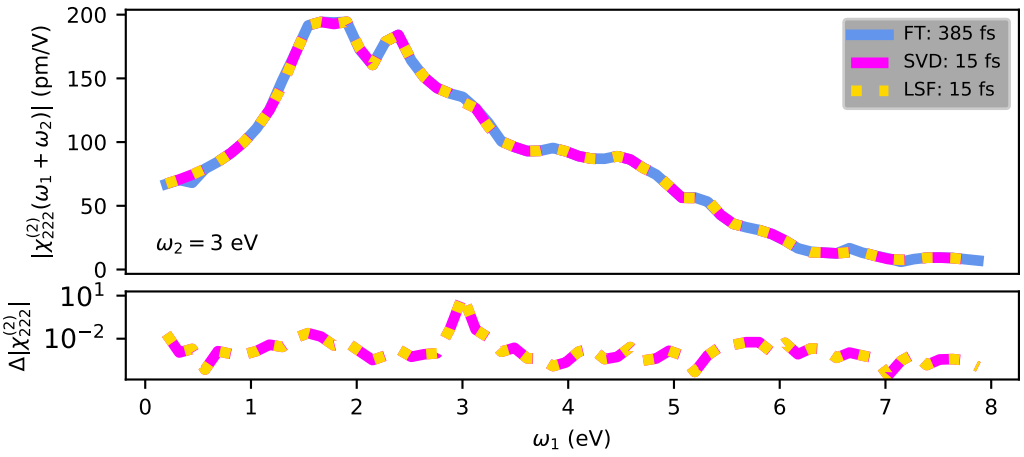

Figure 2: SFG of h-BN with a pump frequency $\omega_2 = 3$ eV obtained at the IPA level using the full discrete Fourier transformation (FT) (blue solid line), singular value decomposition (SVD) (magenta dashed line), and the least square fit (LSF) (yellow dotted line). Results obtained with different sampling times are shown. The discrete FT needs a sampling time (385 fs) about 26 times larger than the SVD and LSF (15 fs). Below is displayed the difference in logarithmic scales for SVD and LSF, respectively, with 5 fs less sampling time to show the convergence.

3.2 Two external monochromatic fields

We consider two monochromatic fields, with commensurate frequencies, ω_1 and ω_2. Frequencies are commensurate as long as they are rational numbers (that is $\omega_1, \omega_2 \in \mathbf{Q}$), which is the case in numerical implementations. The greatest common divisor of ω_1 and ω_2 leads to the fundamental frequency,

$$\omega_0 = \frac{\gcd(\lfloor 10^m\omega_1\rceil, \lfloor 10^m\omega_2\rceil)}{10^m}, \tag{13}$$

where $m = \max(n_1, n_2)$ and n_1 and n_2 are the number of decimals in ω_1 and ω_2, respectively.

The resulting polarization $\boldsymbol{\mathcal{P}}(t)$ is periodic with period $T = 2\pi/\omega_0$ and hence can be written as a Fourier series as in Eq. (11), in terms of the harmonics of ω_0. As the (?) frequencies of the external fields are multiple of the fundamental frequency $\omega_1 = M\omega_0$ and $\omega_2 = N\omega_0$, the $|M \pm N|$ harmonics correspond to the SFG/DFG. When it comes to setting up the system of linear equations (Eq. (12)), the sum over the harmonics must be truncated to an appropriate S to include these processes (that is $S \gtrsim M + N$). When compared with a single external field, the dimension of the system of linear equations is significantly larger. More critically, T can be orders of magnitude larger than typical laser periods in the near-infrared to near-UV range ($\approx 1-5$ fs) for any pair of frequencies with more than one decimal leading to computationally intensive simulations (see Fig. 2).

5 Results

We apply the approach outlined in Secs. 2-3 to the SFG and DFG in h-BN and MoS_2 monolayers (Secs. 5.1-5.2). h-BN monolayer is a wide band gap insulator with strong excitonic features and provides a clear example of the need for an accurate inclusion of excitonic effects. MoS_2 monolayer is one of the most widely studied 2D material, including its SFG/DFG [4, 7]. Since h-BN and MoS_2 monolayer belong to D_{3h} point group [34], they have only one non-vanishing second-order susceptibility tensor element with $\chi^{(2)}_{222} = -\chi^{(2)}_{211} = -\chi^{(2)}_{112} = -\chi^{(2)}_{121} \equiv \chi^{(2)}$[3]. For SFG and DFG, we show results in a heatmap, in which each point has been obtained by a separate real-time simulation. As a guide to reading such heatmaps (see e.g. Fig. 4), we can refer to Eqs. (7)-(8). The susceptibilities corresponding to SFG/DFG have poles both at one-photon ($\omega_{1,2} = \Omega_\lambda$) and at two-photon ($\omega_1 \pm \omega_2 = \Omega_\lambda$) resonances with single-particle transitions (or with excitons) in the system. The one-photon resonances correspond to vertical (ω_1) and horizontal (ω_2) lines in the SFG and DFG heatmaps. In the SFG heatmap, the two-photon resonances correspond to negative slope lines running from $\omega_2 = \Omega_\lambda$ to $\omega_1 = \Omega_\lambda$, while in DFG they correspond to positive slope lines starting at $\omega_2 = \Omega_\lambda$ and $\omega_1 = \Omega_\lambda$. Further, the diagonal $\omega_1 = \omega_2$ corresponds to the SHG in the SFG and the optical rectification in the DFG heatmap. In Sec. 5.3, we consider THz-induced second-harmonic generation in 2L-h-BN. This system has inversion symmetry and thus has zero SHG at zero-field.

5.1 SFG and DFG in h-BN monolayer

In Fig. 4 we report the SFG and DFG spectra for h-BN both at the IPA and TD-aGW approximation level. For SFG, the line $\omega_1 = \omega_2$ corresponds to the SHG, already calculated in Ref. [14]. At the IPA level, the SFG spectrum (Fig. 4(a)) of h-BN is dominated by two-photon resonances with single-particle transitions between 4-6 eV (negative slope bands). In particular, the lowest-energy band corresponds to the transition from the valence band minimum to the conduction band maximum. The one-photon transitions (vertical and horizontal bands) are much weaker though a significant enhancement is observed for part of the spectra both resonant with one- and two-photon absorption. In particular, this portion of the SFG spectrum is twice as intense as the SHG (the $\omega_1 = \omega_2$ diagonal). The DFG spectrum (Fig. 4(b)) is dominated by the resonant optical rectification between 4-6 eV ($\omega_1 = \omega_2$). Further, one-photon resonances (vertical and horizontal bands) are visible, again enhanced when two-photon resonances are also present. These results can be straightforwardly related to the IPA absorption spectrum (see e.g. Ref. [14], which presents a broad peak between 4-6 eV). This broad peak can be found in the calculated absorption spectrum in Fig. 5(a).

As expected, the addition of the electron-hole interaction drastically changes the SFG/DFG spectra[4]. Sharper and much stronger (note the different color scale) features appear in the TD-aGW spectra, corresponding to the E_1, E_2 excitonic peaks at around 6.1 eV and 7 eV [36]. These two excitonic peaks can also be identified in the calculated absorption spectrum at TD-aGW level in Fig. 5(a). Two-photon resonances with the two excitons are clearly visible in the SFG spectrum (negative slope lines in Fig. 4(c)) and DFG spectrum (positive slope lines starting at the exciton energy in Fig. 4(d)). One-photon resonances are also visible (as vertical/horizontal lines). The responses are significantly enhanced in the SFG (DFG) when one laser is resonant with E_1 (E_2) and the second laser

[3] For MoS_2 we have chosen the orientation of the x aligned along an armchair direction following the conventions of Ref. [35].

[4] Note that the shift of the onset is due to the addition of the scissor operator in Table 1 partially compensated by the exciton binding energy.

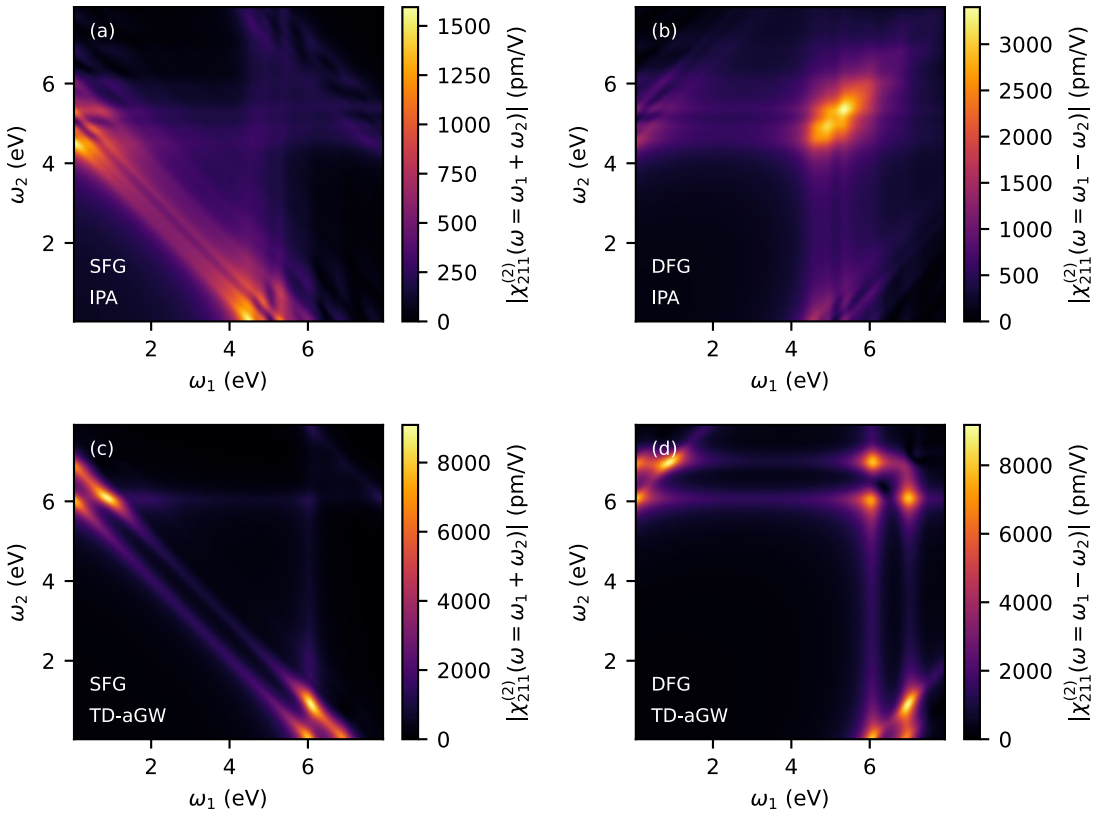

Figure 4: SFG/DFG spectra for h-BN in panels (a), (b) at the independent particle level and in panels (c), (d) at the TD-aGW level. These heatmaps have been generated using a frequency grid of $\omega_1 \times \omega_2 = 96 \times 96$ points. For each frequency pair a real-time simulation was run and the output signal processed.

with $E_2 - E_1$. These spectral features correspond to the first and third terms in Eq. (8) and provide a measure of the strength of exciton-exciton transitions. In the DFG spectrum, strong features are visible as well on the diagonal, corresponding to the exciton-resonant optical rectification, as well as when one laser is resonant with one exciton and the second with the other (corresponding to the second and fourth term in Eq. (8)).
The results presented here on the h-BN monolayer are a proof of concept of our methodology, showing that resonances with strongly bound excitons are important in both SFG/DFG spectra. Due to the large band gap of h-BN, the region of interest for SFG/DFG is difficult to sample and to our knowledge there are no experimental measurements.

5.2 SFG and DFG in MoS_2 monolayer

In Fig. 6, we report the SFG and DFG spectra for the MoS_2 monolayer at the IPA and TD-aGW level. When compared with h-BN, the differences between the IPA and TD-aGW spectra are less striking, as already observed for the absorption [37] and the SHG [14]. Similarly to what was observed for the SHG [14,38,39], a significant enhancement is seen at resonances with the C exciton ($\approx$ 3 eV), while the weaker A and B excitons ($\approx$ 2.2 eV, as spin-orbit coupling is not included the peaks are degenerate) show minimal excitonic enhancement. These excitonic peaks are also visible in the linear absorption spectrum as shown in Fig. 5(b). The SFG spectrum shows a strong two-photon resonance with the C exciton (negative slope line) while the DFG spectrum shows a strong one-photon reso-

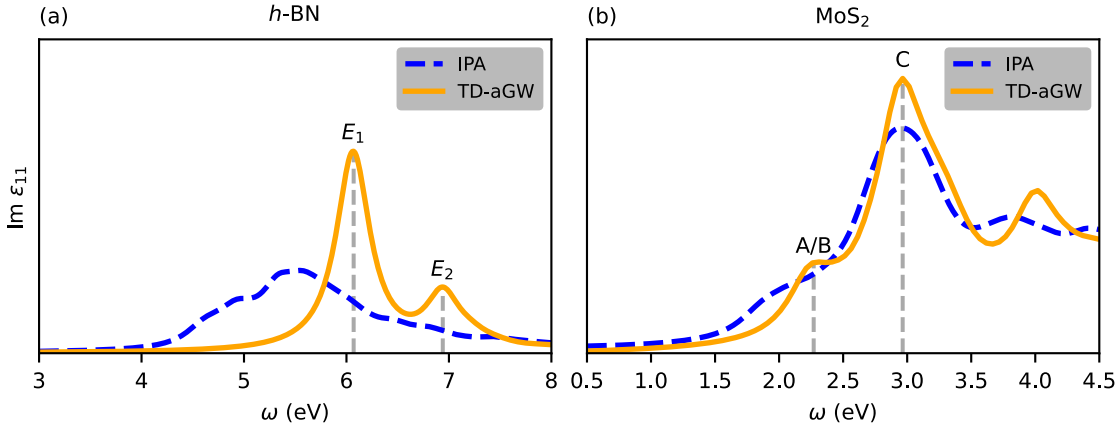

Figure 5: Calculated imaginary dielectric function of (a) h-BN and (b) at the IPA (blue dashed line) and TD-aGW (orange solid line) level. The excitonic peaks E_1 and E_2 of h-BN are located at around 6.1 eV and 7 eV, respectively (panel (a)). The degenerate excitonic peak A/B as well as C can be seen at around 2.2 eV and 3 eV, respectively (panel (b)).

nance (vertical/horizontal line) and a strong exciton resonant optical rectification. Though less evident than for h-BN, there is an enhancement in the intensity in correspondence of exciton-exciton transitions. In the SFG (Fig. 6(c)), the signal is enhanced when one laser is resonant with the A/B exciton (about 2.2 eV) while the frequency of the second matches the energy difference between the C and A/B excitons. In the DFG (Fig. 6(d)), the signal is enhanced when one laser is resonant with the C exciton (about 3 eV) while the frequency of the second corresponds to the energy difference between the C and A/B excitons.

SFG and DFG were measured in mono- [5,7,40,41] and few-layers [4] MoS_2. In the presence of metal substrates [40], excitonic resonances were shown to be strongly attenuated, and their position shifted due to gap renormalization. These effects are beyond the methodology presented in this manuscript. Other measurements are performed in a pump-probe configuration with a delay between the pump and probe [40], which in our case requires the inclusion of dephasing effects that are beyond the scope of the present work. Finally, for insulating substrates and synchronized pump and probe, our simulation results are in agreement with existing measurements. In particular, SFG has been observed [41] at 2.9 eV when laser fields at 1.2 eV and 1.9 eV were injected. The DFG was observed [7] by fixing one laser at 3.06 eV and varying the second between 0.79 and 0.95 eV, showing an enhancement of the signal between 2.1-2.2 eV, which the authors attributed to excitonic effects in this region. Our results support this interpretation.

5.3 Field-induced second-harmonic generation

In Fig. 7 we report the third-order susceptibility corresponding to the FI-SHG in h-BN bilayer. For each frequency ω, we run a real-time simulation in the presence of the THz pump ($\nu = 10$ THz). The response functions reported in the figure correspond to two possible experimental configurations, a pump and probe in the y direction ($\chi^{(3)}_{2222}$), and a pump in the x and probe in y direction ($\chi^{(3)}_{1221}$). In both configurations, susceptibility shows a strong resonance at half of the gap, around 2-3 eV, similar to the standard SHG in h-BN monolayer [14]. We found that the intensity of the response when the pump and probe are

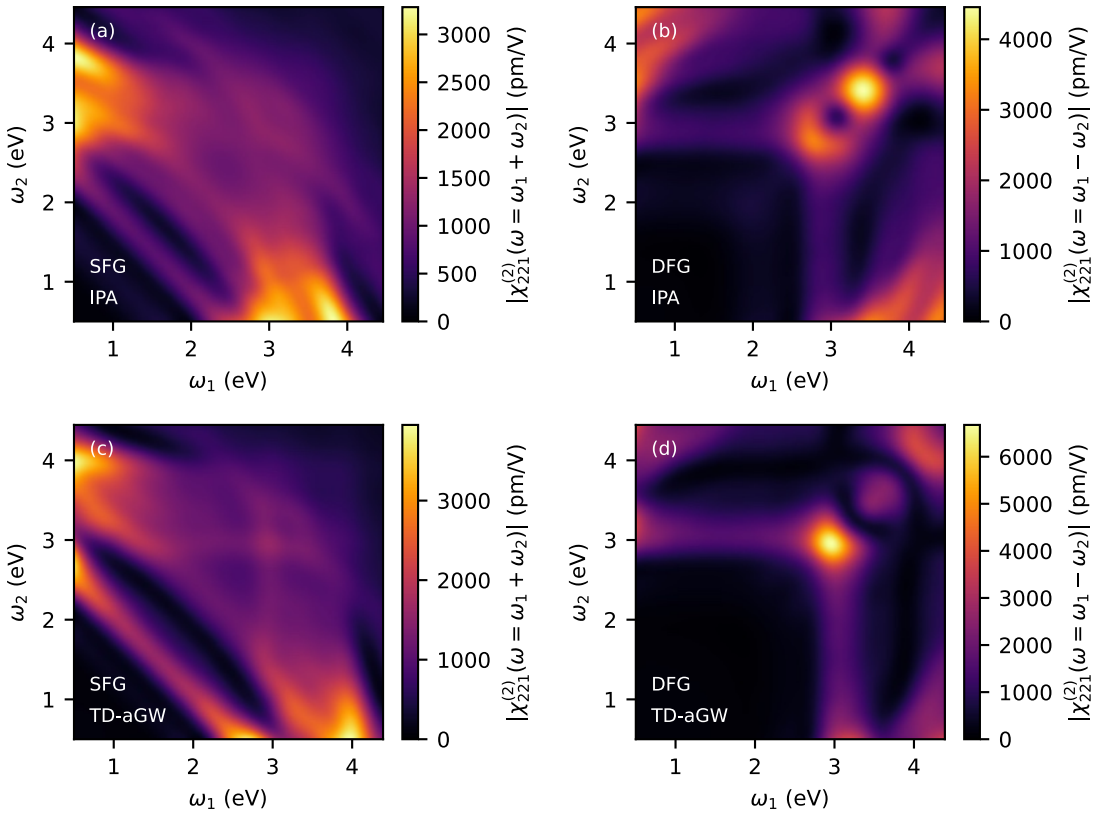

Figure 6: SFG/DFG spectra for MoS_2 in panels (a) and (b) at the independent particle level and in panel (c), (d) at the TD-aGW level. These heatmaps have been generated using a frequency grid of $\omega_1 \times \omega_2 = 96 \times 96$ points for the IPA and $\omega_1 \times \omega_2 = 72 \times 72$ for the TD-aGW. For each frequency pair a real-time simulation was run and the output signal processed.

parallel is higher than that in the perpendicular configuration. The order of magnitude of the $\chi^{(3)}$ is comparable with that of bulk ferroelectric oxides which are known for their excellent nonlinear properties [42]. This result implies that two-dimensional crystals can be used as a detector for THz radiation [43].

6 Conclusions

In this work, we present a computational framework to study sum/difference frequency generation by means of real-time simulations in the presence of multiple laser fields[5]. With multiple fields, the challenge is the signal processing required to extract the non-linear susceptibilities. In particular, using a discrete Fourier transform approach may require very long and thus computationally costly simulations. We found that approaches based either on the singular value decomposition and the least squares optimization give accurate results with short sampling time and allow to reduce significantly the simulation time. These approaches enable the calculation of second-order response functions, such as SFG/DFG, and higher nonlinear response functions, as FI-SHG, including excitonic

[5] After submission, we became aware of a newly published study proposing an alternative approach to the one we have developed [44]. (full stop)

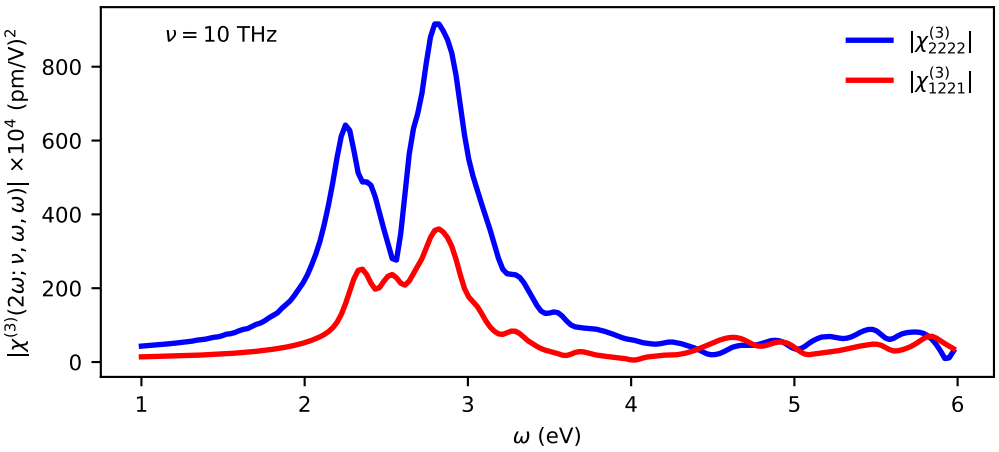

Figure 7: Calculated THz field-induced second-harmonic generation of *h*-BN bilayer with ν=10 THz at the IPA level. Each curve consists of 192 frequency steps between $\omega = 1 - 6$ eV.

effects within many-body theory. For the studied systems, *h*-BN monolayer and MoS_2, we showed that including excitonic effects in SFG/DFG spectra is critical. In both materials, we predict strong features corresponding to exciton transitions, as recently experimentally observed for another layered material [9]. Further, the results on FI-SHG for *h*-BN bilayer demonstrate that the approach can be used to predict and interpret nonlinear terahertz spectroscopy of solids [45]. Finally, the presented approach can be coupled to atomic vibrations using finite displacement methods [46, 47] opening the way to simulate other spectroscopic techniques such as coherent anti-Stokes Raman spectroscopy (CARS). The latter is a powerful nonlinear optical technique for probing vibrational modes in molecular and solid-state structures. CARS involves two laser beams exciting a vibrational state, and a third beam generating a coherent anti-Stokes signal, allowing for high resolution imaging [48]. CARS can be seen as a combination of SFG and DFG processes, and therefore the method shown in this study could be employed to study the nonresonant CARS response. Since the pure nonresonant CARS is not directly available experimentally [49], the *ab initio* real-time simulation is a promising feature to support CARS measurements.

Acknowledgments

The authors gratefully acknowledge financial support from the Deutsche Forschungsgemeinschaft through the FOR5044 research group (ID: 426703838; http://www.For5044.de). Calculations for this research were conducted on the Lichtenberg high-performance computer of the TU Darmstadt and at the Höchstleistungsrechenzentrum Stuttgart (HLRS). The authors furthermore acknowledge the computational resources provided by the HPC Core Facility and the HRZ of the Justus-Liebig-Universität Gießen. C.A. acknowledges B. Demoulin and A. Saul for the management of the computer cluster *Rosa*. C.A. acknowledges the French "Agence Nationale de la Recherche (ANR)" for financial support (Grant Agreement No. ANR-22-CE30-0027). C.A. and M.G. acknowledge funding from European Research Council MSCA-ITN TIMES under grant agreement 101118915 and from AMUtech. M.G. acknowledges funding from the UKRI Horizon Europe Guarantee funding scheme (EP/Y032659/1).